



Full length article

Osteocyte apoptosis and cellular micropetrosis signify skeletal aging in type 1 diabetes



Sofie Dragoun Kolibová^a, Eva Maria Wölfel^{a,b}, Haniyeh Hemmatian^a, Petar Milovanovic^{a,c}, Herbert Mushumba^d, Birgit Wulff^d, Maximilian Neidhardt^{e,b}, Klaus Püschel^d, Antonio Virgilio Failla^f, Annegreet Vlug^g, Alexander Schlaefer^{e,b}, Benjamin Ondruschka^d, Michael Amling^a, Lorenz C. Hofbauer^h, Martina Rauner^h, Björn Busse^{a,b,*}, Katharina Jähn-Rickert^{a,i}

^a Department of Osteology and Biomechanics, University Medical Center Hamburg Eppendorf, Hamburg, Germany

^b Interdisciplinary Competence Center for Interface Research, University Medical Center Hamburg Eppendorf, Hamburg, Germany

^c University of Belgrade, Faculty of Medicine, Center of Bone Biology, Institute of Anatomy, Belgrade, Serbia

^d University Medical Center Hamburg Eppendorf, Institute of Legal Medicine, Hamburg, Germany

^e Institute of Medical Technology and Intelligent Systems, Hamburg University of Technology, Am-Schwarzenberg-Campus 3, Hamburg 21073, Germany

^f University Medical Center Hamburg Eppendorf, UKE microscopy Imaging facility, Hamburg, Germany

^g Leiden University Medical Center (LUMC), Centre for Bone Quality, Leiden, the Netherlands

^h Division of Endocrinology, Department of Medicine III, Technische Universität Dresden Medical Center, Diabetes, and Metabolic Bone Diseases, Dresden, Germany

ⁱ Mildred Scheel Cancer Career Center Hamburg, University Cancer Center Hamburg, University Medical Center Hamburg-Eppendorf, Hamburg 20251, Germany

ARTICLE INFO

Article history:

Received 12 October 2022

Revised 3 February 2023

Accepted 27 February 2023

Available online 4 March 2023

Keywords:

Type 1 diabetes mellitus

Micropetrosis

Osteocyte apoptosis

Cell death

Microdamage accumulation

Skeletal aging

ABSTRACT

Bone fragility is a profound complication of type 1 diabetes mellitus (T1DM), increasing patient morbidity. Within the mineralized bone matrix, osteocytes build a mechanosensitive network that orchestrates bone remodeling; thus, osteocyte viability is crucial for maintaining bone homeostasis. In human cortical bone specimens from individuals with T1DM, we found signs of accelerated osteocyte apoptosis and local mineralization of osteocyte lacunae (micropetrosis) compared with samples from age-matched controls. Such morphological changes were seen in the relatively young osteonal bone matrix on the periosteal side, and micropetrosis coincided with microdamage accumulation, implying that T1DM drives local skeletal aging and thereby impairs the biomechanical competence of the bone tissue. The consequent dysfunction of the osteocyte network hampers bone remodeling and decreases bone repair mechanisms, potentially contributing to the enhanced fracture risk seen in individuals with T1DM.

Statement of significance

Type 1 diabetes mellitus (T1DM) is a chronic autoimmune disease that causes hyperglycemia. Increased bone fragility is one of the complications associated with T1DM. Our latest study on T1DM-affected human cortical bone identified the viability of osteocytes, the primary bone cells, as a potentially critical factor in T1DM-bone disease. We linked T1DM with increased osteocyte apoptosis and local accumulation of mineralized lacunar spaces and microdamage. Such structural changes in bone tissue suggest that T1DM speeds up the adverse effects of aging, leading to the premature death of osteocytes and potentially contributing to diabetes-related bone fragility.

© 2023 The Author(s). Published by Elsevier Ltd on behalf of Acta Materialia Inc.
This is an open access article under the CC BY license (<http://creativecommons.org/licenses/by/4.0/>)

* Corresponding author at: Department of Osteology and Biomechanics, University Medical Center Hamburg-Eppendorf, Lottestr. 55A, Hamburg 22529, Germany.
E-mail address: b.busse@uke.de (B. Busse).

1. Introduction

Diabetes mellitus (DM) represents a significant public health concern, with approximately 537 million adults currently living

with diabetes, and its global prevalence is rising [1]. DM is a chronic metabolic disorder characterized by high blood glucose levels. In type 1 DM (T1DM), accounting for 10% of all diabetes cases worldwide, hyperglycemia is caused by a lack of insulin due to autoimmune-induced damage to pancreatic beta cells [2,3]. The long-term effects of T1DM are tissue and organ damage, including impaired skeletal health involving a significant increase in fracture risk; the relative risk of hip fracture is reported to be as high as 6.94 for individuals with T1DM [4–8]. Bone mineral density (BMD), the general predictor of bone fragility, is reduced in T1DM [9–12]. However, the reported increase in fracture risk cannot be explained solely by the reduction in BMD; thus, there is a need to identify novel markers of reduced mechanical competence of bone.

It is thought that decreased bone turnover contributes to diabetic bone disease [13]. Bone turnover is accomplished through the bone remodeling process, in which the central regulatory cells, osteocytes, orchestrate bone-resorbing osteoclasts and bone-forming osteoblasts in response to mechanical loading. The cellular processes of bone remodeling are coupled in a spatiotemporal sequence by a functional osteocyte network to maintain bone tissue homeostasis or adapt to changing mechanical or hormonal environments [14].

Osteocytes are the most abundant bone cells, forming a mechanosensory and force-translating network within the mineralized bone matrix [15]. Each osteocyte forms approximately 90 dendrites [16], long cytoplasmic extensions that run through nanoscale canals (canaliculi) and enable the connection of osteocytes to each other and to other cells at the periosteum or in the bone marrow cavity, resulting in an extensive communication system called a lacunar (harboring the cell body)-canalicular network (LCN). As postmitotic cells, osteocyte viability [17] is crucial for the maintenance of bone homeostasis. Through a functional fluid-filled LCN, nutrients and waste products are transported to preserve osteocyte viability and maintain their mechanosensory function.

The lifespan of osteocytes is thought to be between 1 and 50 years, starting from a subpopulation of osteoblasts that become embedded into their newly formed bone matrix and differentiate into dendritic osteocytes, ultimately ending in one of the known cell death mechanisms. Osteocyte cell death becomes more prominent with aging [18] but is also associated with multiple bone pathologies, i.e., postmenopausal osteoporosis, glucocorticoid-induced osteoporosis [19,20], or immobilization [21], which are all characterized by elevated bone fragility and therefore higher fracture risk. The fragility is likely caused by a decreased ability to sense and repair microdamage in the bone matrix. In a physiological state, osteocyte apoptosis induces local bone resorption, resulting in the removal of damaged bone matrix, and coupled bone formation ensures the renewal of the bone matrix and the osteocyte cell pool [22,23]. The phenomenon of osteocyte lacunar mineralization, also known as micropetrosis, reflects the decreased number of osteocytes due to cell death and lack of newly embedded osteocytes during bone formation seen with bone pathologies [24]. Micropetrosis negatively affects the mechanical properties of bone tissue, lowering energy absorption and dissipation capacities and thereby causing the bone matrix to become more susceptible to fragility fractures [17,25–27]. An impaired osteocyte network in the form of lower numbers of viable interconnected osteocytes leads to a reduced recognition of microdamage within the bone matrix [28].

Microdamage removal requires communication between apoptotic osteocytes at the site of damage and adjacent nonapoptotic osteocytes, which subsequently activate the osteoclastogenic signaling response for local bone remodeling [29]. The accumulation of microdamage, such as microcracks, creates morphological changes in the LCN, which induce osteocyte apoptosis [30,31]. These effects induce osteoclast-dependent resorption of the dam-

aged bone matrix as a part of functional bone homeostasis. However, when the rate of osteocyte apoptosis exceeds osteocyte viability or when bone resorption is lowered or less targeted (i.e., due to reduced activation by osteocytes), bone resistance to fracture decreases. In a streptozotocin-induced rat model of T1DM, the accumulation of microdamage after ulnar loading led to a severe disruption of the LCN and reduced osteoclast activation, causing a reduction in bone resorption [32]. Because studies with human bone specimens are rare, it is yet unknown whether and to what extent there is microdamage accumulation in the bone matrix of human individuals with T1DM and if it characterizes diabetic bone pathology.

We investigated the effect of T1DM on human femoral cortical bone using an interdisciplinary approach, applying clinical imaging (e.g., microcomputed tomography) and standardized bone histological methods (e.g., bone histomorphometry), material-based techniques (e.g., quantitative backscattered electron microscopy), and novel imaging approaches to detect and quantify microdamage accumulation. We hypothesized that T1DM would promote osteocyte apoptosis, which would affect the integrity of the LCN and result in the accumulation of microcracks in T1DM-induced bone disease.

2. Materials and methods

2.1. Study design

We evaluated the influence of T1DM on bone microarchitecture, matrix quality, and cellular parameters of cortical bone. We collected approximately 1.5-cm-thick bone specimens from the femoral mid-diaphysis of 22 human donors of both sexes for cortical bone quality analysis. The specimens were obtained in collaboration with the Institute of Legal Medicine at University Medical Center Hamburg-Eppendorf (ethics approval: WT037/15). According to medical records, donors were divided into two study groups, including a group of eight donors diagnosed with T1DM (T1DM group: 55.0 ± 10.6 years) during their lifetime and a group of 14 age-matched healthy donors (control group: 53.1 ± 9.5 years) with normal sugar metabolism. For each donor, we collected deidentified patient data (age, BMI) and BMD measured via *ex vivo* DXA measurement of the 12th thoracic vertebra (Table 1). Donors in this study did not suffer from any form of bone disease (i.e., trauma, osteogenesis imperfecta, Paget's disease, fibrous dysplasia, or malignancy).

Femoral bone specimens were fixed in 4% paraformaldehyde (Sigma-Aldrich, Darmstadt, Germany) for 7 days. From the fixed specimens, several 4-mm-thick sections were cut out using a diamond belt saw (EXAKT Advanced Technologies GmbH, Norderstedt, Germany) followed by imaging the whole cross-sections in a cabinet X-ray system. The anterior quadrant was extracted from each cross-section and additionally fixed in 4% paraformaldehyde (Sigma-Aldrich, Darmstadt, Germany) overnight before embedding in methyl methacrylate (MMA). The anterior quadrant from another cross-section was cut and decalcified for six weeks in a 20% ethylenediaminetetraacetic (EDTA) solution prior to paraffin embedding for immunohistochemistry (IHC). The methodology of the study is summarized in Supplemental Fig. 9. All analyses were performed in a blinded manner.

2.2. Microcomputed tomography

The microstructure of the anterior quadrant was assessed using microcomputed tomography (μ CT 40, Scanco Medical AG, Switzerland) at a spatial resolution of $10 \mu\text{m}$. The X-ray settings were standardized to 55 kV and 145 μA with an integration time of 200 ms. A threshold of 550 mg HA/cm^3 was applied to assess cortical porosity (Ct. Po) and tissue mineral density (TMD) using Scanco

Table 1
Cohort characteristics.

	Control <i>n</i> = 14	T1DM <i>n</i> = 8	<i>p</i> value
Age (years)	51 ± 34 ^b	52 ± 31 ^b	0.603
Sex (m/f)	12/2	6/2	0.602
BMI (kg/m ²)	29 ± 14 ^b	22 ± 38 ^b	0.127
Ex vivo BMD of 12 th thoracic vertebra (g/cm ²)	AP: 0.9 ± 0.2 ^a LAT: 0.7 ± 0.1 ^a	AP: 0.8 ± 0.1 ^a LAT: 0.6 ± 0.2 ^a	0.191 0.390

Notes: The table summarizes the information on age, sex, BMI, and ex vivo BMD of the 12th thoracic vertebra (T12) for the control and T1DM groups. Data are presented as the mean ± standard deviation for normally distributed data (marked with a superscript “a”), and nonnormally distributed data are presented as the median ± interquartile range (marked with a superscript “b”). A *t* test was applied for normally distributed data to determine *p* values, and the Mann–Whitney test was used for nonnormally distributed data. Fisher’s exact test was applied to determine the *p* value for sex distribution. BMI: body mass index, BMD: bone mineral density, AP: anterior–posterior, LAT: lateral.

image processing software. Cortical thickness (Ct. Th) was calculated from the contact radiography images within the whole cross-section of the femoral diaphysis using ImageJ/Fiji software (NIH, USA).

2.3. Geometric analysis

Biomechanical properties, such as diaphyseal strength and rigidity, depend upon geometric indices of the femoral diaphysis. To evaluate bone geometry indices, the whole cross-sectional area of the midshaft femur was visualized by contact radiography (Faxitron MX-20, Faxitron, Arizona, USA). The images were analyzed using the EPJ macro [33] in ImageJ/Fiji. The EPJ macro derives periosteal and endosteal contours from images and computes the following cross-sectional properties: total cross-sectional area (TA, mm²), which reflects resistance to compression; cortical area (CA, mm²), which indicates compressive/tensile strength; medullary cavity area (MA, mm²); percent cortical area (%CA, %), which is determined as (CA/TA) × 100; second moment of area, which indicates bending rigidity in the medial–lateral axis (I_x, mm⁴) and anterior–posterior axis (I_y, mm⁴); maximum and minimum second moment of area, which indicate maximum bending rigidity (I_{max}, mm⁴) and minimum bending rigidity (I_{min}, mm⁴), respectively; section modulus, which indicates resistance to bending along the medial–lateral axis (Z_x, mm³) and anterior–posterior axis (Z_y, mm³); and buckling ratio (BR), which indicates resistance to buckling.

2.4. Cellular histomorphometry

For cellular histomorphometry, we cut 5 μm-thick sections from MMA blocks on a microtome (Leica Microsystems, Wetzlar, Germany) and stained the sections with toluidine blue. A total bone area of 1.875 mm² in the endocortical region and a total bone area of 0.625 mm² in the periosteal region were analyzed using Osteomeasure software (Osteometrix, Atlanta, USA). Histomorphometric variables are derived from primary measurements such as bone area or perimeter. These parameters are presented as the source (the structure on which the measurement is made), the measurement, and the referent (source-measurement/referent), in accordance with the ASBMR nomenclature guidelines [34]. The histomorphometric variables were as follows. Bone formation indices: number of osteoblasts per unit bone perimeter (N.Ob/B.Pm; #/mm); osteoblast surface (Ob.S/BS): percent of bone surface occupied by osteoblasts; osteoid volume (OV/BV; %): percent of a given volume of bone tissue that consists of unmineralized bone (osteoid); osteoid surface (OS/BS; %): percent of bone surface covered in osteoid; osteoid thickness (O.Th): mean thickness, provided in micrometers for osteoid bone. Bone resorption indices: number of osteoclasts per unit bone perimeter (N.Oc/B.Pm; #/mm); osteoclast surface (Oc.S/BS): percent of bone surface occupied by osteoclasts;

eroded surface (ES/BS; %): percent of bone surface occupied by resorption cavities with or without osteoclasts.

2.5. Bone mineral density distribution

To evaluate the bone mineral density distribution (BMDD) and 2D morphological analysis of the osteocyte lacunae, we performed quantitative backscattered electron imaging. The PMMA-embedded specimens were subjected to coplanar grinding and subsequently polished and carbon-coated before imaging. A scanning electron microscope (Crossbeam 340, GeminiSEM, Zeiss AG, Oberkochen, Germany) in backscattered electron mode was operated at 20 keV with a constant working distance of 20 mm. A Faraday cup was used to control the current beam, and grayscale values were calibrated using an aluminum–carbon standard. All parameters were monitored during imaging and kept at a constant level. The magnification used for acquiring images was 250x, corresponding to 1 μm/pixel. Two images per region were taken for BMDD and osteocyte lacunae morphology analysis. The total mean calcium content of the BMDD (CaMean, wt%) was assessed from the backscattered electron images using a custom-made MATLAB code (MATLAB, Natick, Massachusetts). We evaluated BMDD in the endocortical and periosteal regions separately. Additionally, we manually created masks in ImageJ/Fiji to separate the osteonal and interstitial areas, and we assessed BMDD for these two areas separately. For this purpose, osteonal bone was defined as a circular region of bone matrix surrounding a Haversian canal; interstitial bone was defined as bone matrix between the circular osteonal structures. Cement lines were used as visual borders for the measurement of bone matrix area.

2.6. Supervised deep learning to detect osteocyte lacunae

To analyze the occurrence of mineralized osteocyte lacunae (Mn.Lc. N), we used images acquired for BMDD on a scanning electron microscope (Crossbeam 340, GeminiSEM, Zeiss AG, Oberkochen, Germany). We trained a deep convolutional neural network (CNN) to detect and classify lacunae as nonmineralized, partially mineralized, or fully mineralized using a pretrained YOLOv5 [35] model as a single-stage object detection algorithm. The model was adapted for the detection of lacunae by training in an end-to-end fashion on lacunae in 50 expert-labeled images. Overall, 8716 nonmineralized, 314 partially mineralized, and 394 fully mineralized lacunae were labeled. We used 10-fold cross-validation to train and validate the model’s performance. For each iteration, we split our data into 40 images for training (80%), 5 images for validation (10%), and 5 excluded images (10%) for testing. To leverage the data set, we performed random horizontal and vertical flipping and rotation followed by random cropping into patches of 256 × 256 pixels, which resulted in a total data set of 7500 patches. We trained the model using stochastic gradient descent with a learning rate of 0.01, a batch size of 324, and 200 epochs;

we report the mean average precision (mAP) metric for all 10 iterations with an intersection over the union threshold of 50%. The network performance was evaluated exclusively on the test set. For further statistical evaluations, we used all available images. Detected artifacts were cleared from the output image data, and we distinguished the locations of micropetrotic lacunae within the osteonal and interstitial areas in the endocortical and periosteal regions. We normalized the number of partially mineralized and fully mineralized lacunae and the total number of mineralized osteocyte lacunae to the mineralized bone area (B.Ar; #/mm²) for evaluation.

2.7. Osteocyte apoptosis

For osteocyte apoptosis detection, a TUNEL assay, allowing visualization of DNA breaks, was used. The plastic embedding medium was washed out from the undecalcified MMA sections using xylene, and the sections were rehydrated by a descending ethanol series (absolute, 90%, 80%, and distilled water). Following 20 minutes at room temperature (RT) of incubation with proteinase K, the sections were treated with 20% EDTA for 30 minutes at 37 °C. The pretreated sections were then stained using fluorescein from an *In Situ* Cell Death Detection Kit (Roche, Basel, Switzerland) overnight at 37 °C. After staining, the sections were washed with phosphate-buffered saline (PBS) solution and treated with a permeabilization solution with 0.1% Triton X-100 and 0.1% sodium citrate for 8 minutes at RT. The samples were then mounted using mounting medium with DAPI stain. The excitation wavelength for visualization was between 450 nm and 500 nm, while detection was between 515 nm and 568 nm. We acquired five images in the periosteal and endosteal regions in the blue and green channels. For evaluation, ImageJ software was used to merge both fluorescent images, and only cells where the signal from both channels was firmly overlapping were counted as apoptotic. We counted viable and apoptotic osteocytes per bone area (B.Ar; #/mm²) in the endocortical and periosteal regions.

Caspase-3 is one of the main “executioners” in cell apoptosis. Therefore, IHC staining for caspase-3 is recommended to detect and quantify apoptosis in tissue sections [36,37]. Decalcified sections were deparaffinized using xylene and rehydrated by a descending ethanol series (absolute, 90%, 80%, and distilled water). We performed enzymatic antigen unmasking by 20 min of incubation at RT with Proteinase K and subsequent treatment with 20% EDTA for 30 min at 37 °C. For staining, we used a SignalStain® Apoptosis Cleaved Caspase-3 Detection Kit (Cell Signaling Technology, Danvers, MA, United States). The pretreated sections were then stained in accordance with the manufacturer’s recommendation overnight at 4 °C. After incubation, the sections were washed, and apoptotic cells were detected by the 3,3-diaminobenzidine (DAB) chromogen (DAKO, Carpinteria, CA, USA) for approximately 8 min. Finally, the slides were counterstained in hematoxylin for 1 s, washed in distilled water, dehydrated, and mounted. The slides were imaged using a PANNORAMIC MIDI Digital Slide Scanner (Sysmex Corporation, Kobe, Hyogo, Japan) at a 60 × objective magnification. We analyzed a total bone area of 1 mm² for the endosteal region and 2 mm² for the periosteal region. The apoptotic cells were counted manually using an object-counting tool in Olympus cellSens software (Shinjuku City, Tokyo, Japan). We quantified the total number of apoptotic osteocytes per bone area (B.Ar; #/mm²) in the endocortical and periosteal regions.

2.8. Microcrack accumulation

To investigate microcrack accumulation, we used infiltration with rhodamine-6G and confocal laser scanning microscopy [38]. The advantage of this approach is infiltration with rhodamine-6G

before embedding, meaning that only the existing cracks are labeled, and no artifacts created during the embedding process are stained. From the fixed femoral cross-sections, we cut out the region next to the anterior quadrant in a lateral direction using a diamond belt saw (EXAKT Advanced Technologies GmbH, Norderstedt, Germany) to obtain a 10 mm bone piece. The specimens were dehydrated by an ascending ethanol series and infiltrated for 10 days with 0.002% WT rhodamine-6G before being embedded in MMA. The embedded specimens were then ground to 1 cm to fit into the imaging chamber with a glass bottom. Using a confocal laser scanning microscope (Leica SP5, Leica Microsystems, Wetzlar, Germany), we imaged microcracks with a 561 nm laser excitation wavelength at a 20 × objective magnification. For each periosteal and endosteal region, two Z-stacks of fifty images were acquired with a 1 μm distance between images. We quantified the following parameters in ImageJ/Fiji to assess linear microdamage accumulation: total number of linear microcracks per mineralized bone area (B.Ar; #/mm²) and total length of linear microcracks per mineralized bone area (B.Ar; μm/mm²). Microcracks derived from the main branch were counted as microcrack branching.

2.9. Statistical analysis

All analyses were performed using Prism 9 software (GraphPad, San Diego, California). The Shapiro–Wilk test assessed the normality of the data. To analyze whether the studied bone parameters differed between the two groups (control and T1DM), we used an unpaired two-tailed t test for normally distributed data or a non-parametric Mann–Whitney test for nonnormally distributed data, and we analyzed the endocortical and periosteal regions separately. For the evaluation of BMDD parameters, we used ANOVA for repeated measures to evaluate the effect of the group (between-subject factor: control vs. T1DM) and area (within-subject factor: osteonal vs. interstitial bone), as well as their interaction. To compare endocortical and periosteal regions, we used a two-sided paired t test for normally distributed data and a Wilcoxon test for nonnormally distributed data, followed by a Bonferroni correction. Data from the comparison between the endocortical and periosteal regions are shown in the supplemental material. Simple linear regression was used to evaluate the relationship between calcium content and the number of mineralized lacunae per bone area. We used the ROUT method to identify potential outliers with Q = 1%. A two-tailed alpha level below 0.05 was set to identify statistically significant results (**p* < 0.05).

3. Results

3.1. Caspase-3 immunostaining reveals an elevated number of apoptotic osteocytes in cortical bone from individuals with T1DM

Within our T1DM cohort (Table 1), we did not observe any effect of T1DM on the geometric properties of the midshaft femoral cortical bone compared to the control, including neither elevated cortical porosity nor cortical thickness (Supplemental Table 1 and Supplemental Fig. 1). In addition, bone histomorphometry reflected the low bone remodeling rate that is generally seen in cortical bone and did not show any group-specific differences (Supplemental Table 2 and Supplemental Fig. 2). Histomorphometric analysis of osteocytes (Supplemental Fig. 2H) and empty lacunae (Supplemental Fig. 2I) showed similar results for both groups in both regions (Supplemental Table 2). We noted that 40%–50% of the osteocyte lacunae were already empty in both study groups and both of the analyzed bone regions, possibly decreasing the detection of apoptotic osteocytes.

We assessed signs of osteocyte apoptosis as a means of determining osteocyte viability (Fig. 1A, B). With the terminal deoxynu-

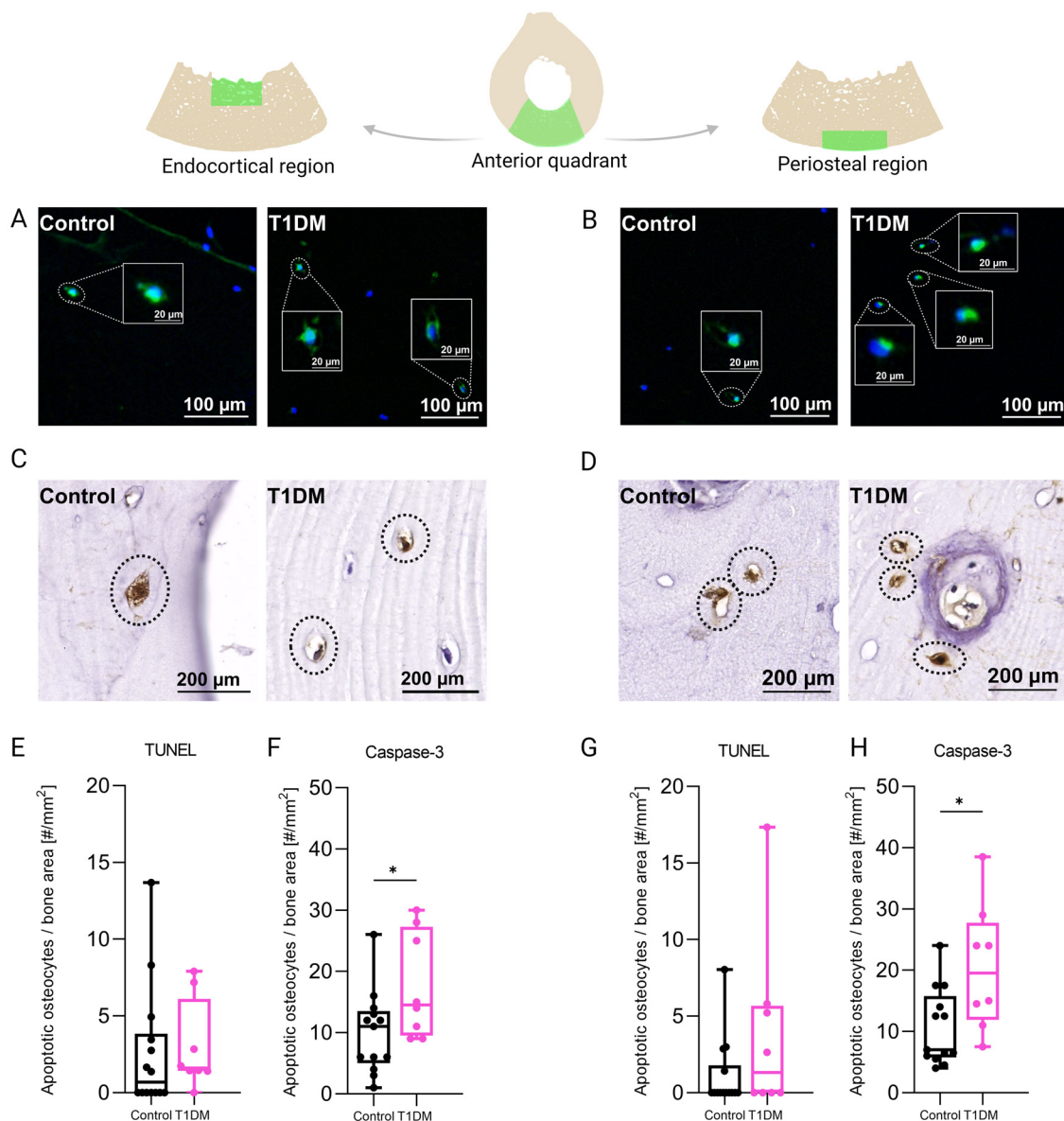


Fig. 1. T1DM promotes osteocyte apoptosis in cortical bone of the femoral mid-diaphysis. Representative images of apoptotic osteocytes stained with TUNEL (A) endocortical and (B) periosteal regions of the control and T1DM groups. Representative images of caspase-3 IHC showing apoptotic osteocytes highlighted by black circles in (C) endocortical and (D) periosteal regions of the control and T1DM groups. (E, G) The results from osteocyte apoptosis detection using TUNEL labeling (endocortical: $p = 0.322$ and periosteal: $p = 0.239$). (F, H) Caspase-3 IHC staining results show a significantly higher number of apoptotic osteocytes in T1DM (endocortical: $p = 0.035$ and periosteal: $p = 0.013$). Boxplots represent the minimum, 25th percentile, median, 75th percentile, and maximum. A t test was applied for normally distributed data to determine p values, and the Mann-Whitney test was used for nonnormally distributed data. * $p < 0.05$.

cleotidyl transferase dUTP nick-end labeling (TUNEL) assay, DNA fragmentation (one hallmark of apoptosis) was labeled, thereby identifying apoptotic osteocytes in human cortical bone. The number of apoptotic osteocytes was normalized to the analyzed cortical bone area for the evaluation. The results showed a comparable number of TUNEL-positive lacunae per bone area between the control and T1DM groups in the endocortical ($p = 0.322$; Fig. 1C) and periosteal regions ($p = 0.239$; Fig. 1E). However, we also employed caspase-3 staining—a more sensitive technique that also detects earlier stages of apoptosis [37]. Caspase-3 IHC staining showed a higher occurrence of apoptotic osteocytes per bone area in then T1DM group than for the control group for both the endocortical region ($p = 0.035$; Fig. 1D) and the periosteal region ($p = 0.013$; Fig. 1F).

3.2. Increased abundance of fully mineralized osteocyte lacunae in the periosteal cortex of T1DM individuals

Mineralization of the osteocyte lacunae (micropetrosis) is the final morphological state of osteocytes undergoing cell death. We visualized osteocyte lacunae undergoing mineralization with high-resolution quantitative backscattered electron imaging (Fig. 2A, B) and determined the number of partially and fully mineralized lacunae per bone area to demonstrate the longitudinal process of micropetrosis (Fig. 2C–F). To evaluate lacunar mineralization, a deep learning model specifically trained on this data set was used to distinguish and count empty, partially mineralized, and fully mineralized lacunae. The custom-made deep learning algorithm achieved $\text{mAP} = 0.77 \pm 0.07$. Empty lacunae, partially mineralized lacunae and fully mineralized lacunae were correctly classified in 95.7%,

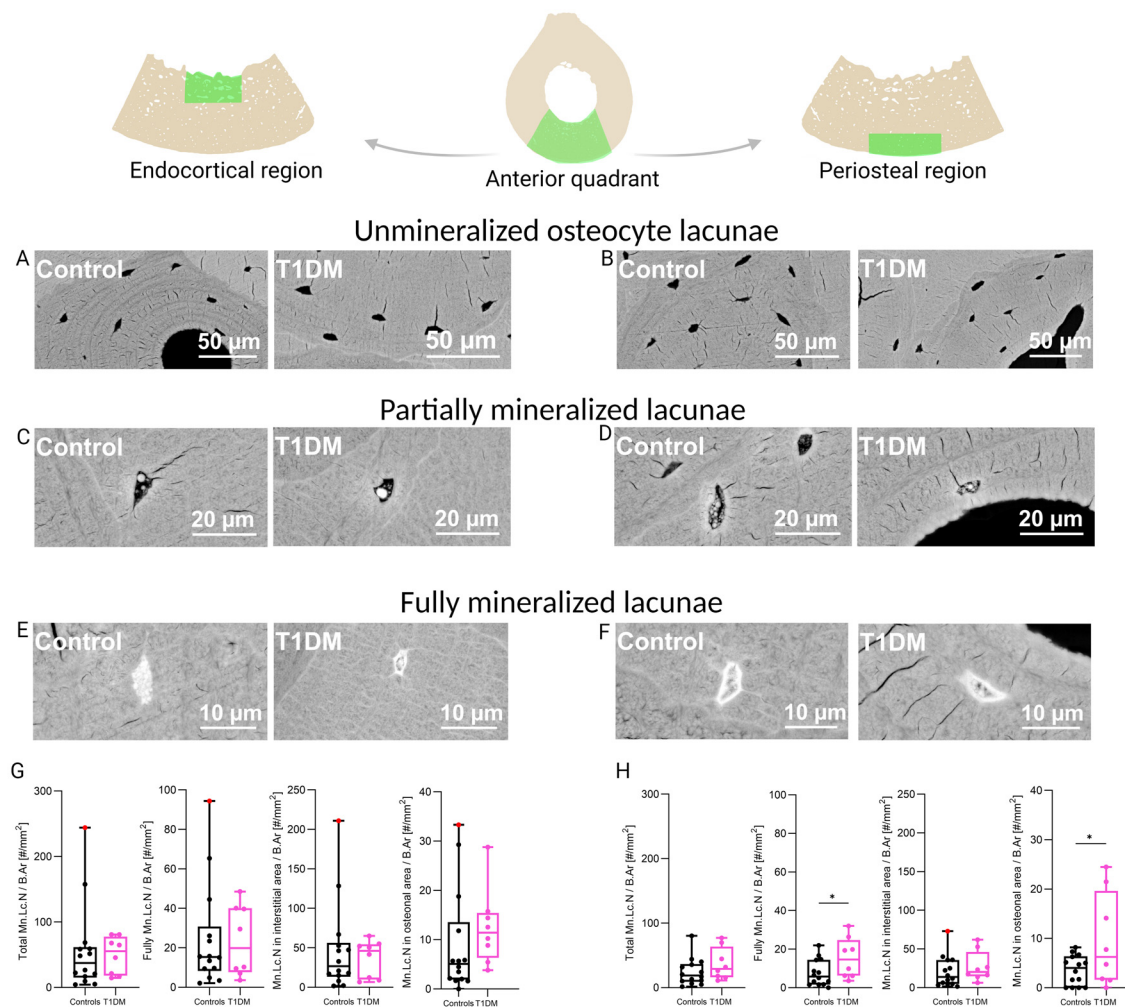


Fig. 2. Osteocyte viability is altered in the periosteal region in the T1DM group. High-resolution backscattered scanning electron microscopy allows the detection of osteocyte lacunae undergoing the mineralization process (micropetrosis), which reflects the viability of osteocytes in cortical bone. Representative images of typical osteocyte lacunae in the (A) endocortical and (B) periosteal regions of the control and T1DM groups. After osteocyte cell death, the lacuna gradually fills with mineral occlusions. Partially filled lacunae are identified by clearly visible calcified nanospherites or by a white halo on the lacunar edges and reflect an intermediate step toward fully mineralized lacunae. Partially filled lacunae are visible in images from the (C) endocortical and (D) periosteal regions for the control and T1DM groups. The last stage of micropetrosis is complete filling of lacunae with calcified nanospherites. Fully mineralized lacunae are shown from the (E) endocortical and (F) periosteal regions for the control and T1DM groups. (G) The analysis of mineralized lacunae in the endocortical region showed comparable values between control and T1DM group in following parameters: total number of mineralized lacunae per bone area (Total Mn.Lc.N/B.Ar; partially and fully mineralized lacunae; $p = 0.570$); number of fully mineralized lacunae per bone area (Fully Mn.Lc.N/B.Ar; $p = 0.868$); number of mineralized lacunae per interstitial bone area (Mn.Lc.N/B.Ar in interstitial area; $p = 0.920$); number of mineralized lacunae per osteonal bone area (Mn.Lc.N/B.Ar in osteonal area; $p = 0.145$). (H) The analysis of mineralized lacunae in the periosteal region revealed a significantly higher number of Fully Mn.Lc.N/B.Ar ($p = 0.046$) and Mn.Lc.N/B.Ar in osteonal area ($p = 0.041$) in T1DM group compared to control specimens. Total Mn.Lc.N/B.Ar ($p = 0.212$) and Mn.Lc.N/B.Ar in interstitial area ($p = 0.297$) was unchanged in control and T1DM groups. For abbreviations see G. Boxplots represent the minimum, 25th percentile, median, 75th percentile, and maximum. Red circles denote identified potential outliers using the ROUT method with $Q = 1\%$. A t test was applied for normally distributed data to determine p values, and the Mann-Whitney test was used for nonnormally distributed data. $*p < 0.05$.

70.2%, and 78.2% of cases, respectively. The confusion matrix and example predictions with the confidence score for the endocortical region and periosteal region are shown in Supplemental Fig. 3.

The total number of micropetrotic lacunae per bone area did not differ significantly between the control and T1DM groups in either the endocortical ($p = 0.570$, Fig. 2G) or the periosteal region ($p = 0.212$, Fig. 2H). The number of fully mineralized lacunae, however, was significantly higher in the T1DM group than in the control group in the periosteal region ($p = 0.046$; Fig. 2G), while no such difference was evident in the endocortical region ($p = 0.868$, Fig. 2H). Furthermore, only in the osteonal area did the number of micropetrotic osteocytes per bone area show intergroup differences in the periosteal region, with more micropetrotic osteocytes in T1DM than in the control group ($p = 0.041$; Fig. 2G); the numbers were similar in the endocortical region ($p = 0.145$; Fig. 2H). This difference between the control and T1DM groups was not ev-

ident in the interstitial area in either the endocortical ($p = 0.920$, Fig. 2G) or the periosteal region ($p = 0.297$; Fig. 2H).

3.3. Cortical bone calcium density distinguishes younger osteonal bone and older interstitial bone in both the T1DM and control groups

Calcium is the most abundant inorganic element in the mineralized bone matrix. Its amount and distribution affect tissue hardness and therefore the local mechanical properties of the bone tissue. The mean calcium weight percentage did not differ between the control and T1DM groups in either the endocortical region ($p = 0.412$) or the periosteal region ($p = 0.551$). Subdivision into the osteonal and interstitial areas did not reveal differences in calcium content between the control and T1DM groups in either the endocortical ($F(1,13) = 0.494$; $p = 0.495$, Fig. 3C) or the periosteal region ($F(1,13) = 0.099$; $p = 0.757$, Fig. 3D). However, in both study

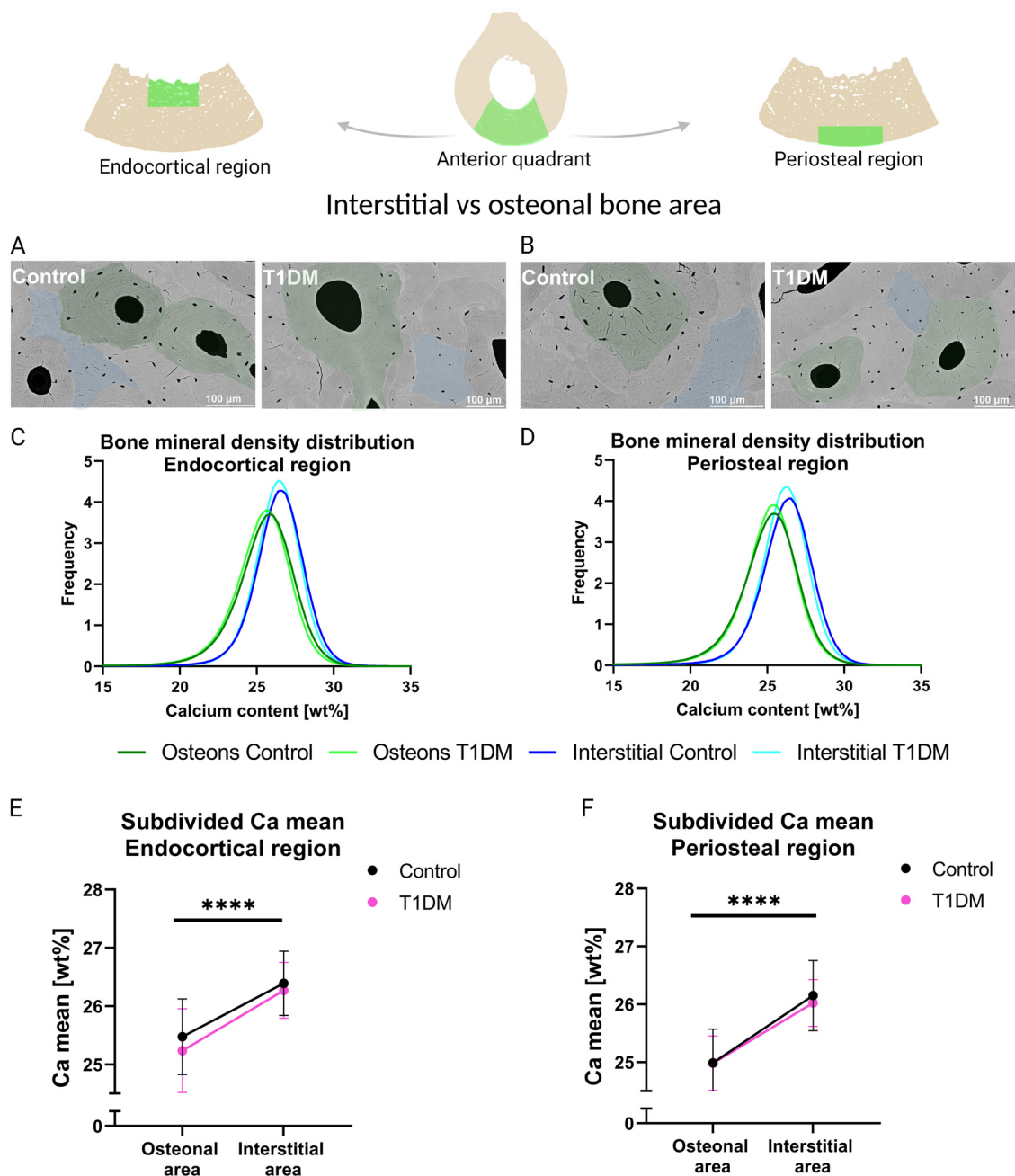


Fig. 3. Bone mineral density distribution is not altered in T1DM. The grayscale level in the images is quantitatively related to the mineral content. Therefore, regions with higher mineral content appear brighter (interstitial areas), while those with lower mineral content appear darker (osteonal areas). A highly mineralized cement line visible as a white contour in the images creates an interface between the osteonal and interstitial areas. High-resolution quantitative backscattered electron images from the control and T1DM groups in the (A) endocortical and (B) periosteal regions, with highlighted examples of the osteonal area in blue and the interstitial area in green. Graphs of the frequency distribution illustrate the distribution of minerals, showing a higher calcium content in the interstitial area than in the osteonal area in both the control and T1DM groups in the (C) endocortical and (D) periosteal regions. The mean calcium weight percentage (Ca mean, wt%) is derived from the grayscale images. The osteonal area consistently showed a significantly lower Ca mean than the interstitial area in both the (E) endocortical and (F) periosteal regions in the control and T1DM groups. Comparison of bone areas (osteonal vs. interstitial) by repeated-measures ANOVA. **** $p < 0.001$.

groups, we observed a consistently lower degree of mineralization in the osteonal bone area than in the interstitial area for both the endocortical ($F(1,13) = 159.3$; $p < 0.0001$, Fig. 3E) and periosteal ($F(1,13) = 65.24$; $p < 0.0001$, Fig. 3F) regions, indicating that the tissue age of the osteonal area was younger than that of the interstitial area in both groups.

3.4. Greater microcrack accumulation and microcrack length in the periosteal femoral cortex in the T1DM group

Rhodamine-6G-infiltrated bone specimens were visualized using confocal microscopy to determine microcrack occurrence in the endocortical (Fig. 4A) and periosteal regions (Fig. 4B). To evalu-

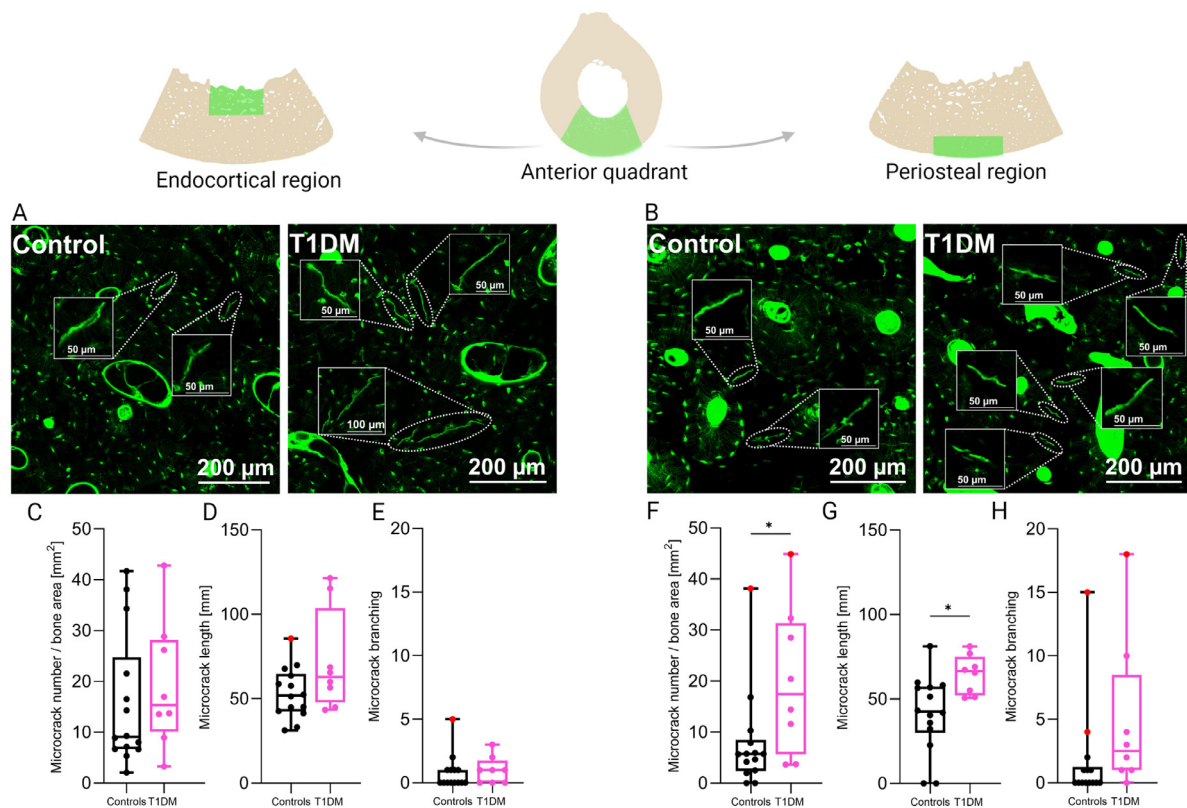


Fig. 4. Microcrack accumulation and total microcrack length in the periosteal region are higher in the T1DM group than in the control group. Rhodamine-6G-infiltrated bone specimens were visualized using confocal laser scanning microscopy. Representative images of linear microcracking in (A) endocortical and (B) periosteal regions of the control and T1DM groups. Confocal imaging results, including the (C, F) number of linear microcracks per bone area (endocortical: $p = 0.365$ and periosteal: $p = 0.048$), (D, G) microcrack length per bone area (endocortical: $p = 0.165$ and periosteal: 0.015), and (E, H) microcrack branching as microcracks derived from the main branch (endocortical: $p = 0.720$ and periosteal: $p = 0.059$). Boxplots represent the minimum, 25th percentile, median, 75th percentile, and maximum. Red circles denote identified potential outliers using the ROUT method with $Q = 1\%$. A t test was applied for normally distributed data to determine p values, and the Mann-Whitney test was used for nonnormally distributed data. $*p < 0.05$.

ate microdamage accumulation, the number of microcracks and microcrack length were normalized to the mineralized bone area. Confocal imaging results showed no effect of T1DM on the number, length or branching of microcracks in the endocortical region (Fig. 4C–E). In contrast, a higher number of linear microcracks per unit bone area in the T1DM group than in the control group was seen in the periosteal region ($p = 0.048$; Fig. 4F). Additionally, the difference in total microcrack length between the T1DM and control groups in the periosteal region was statistically significant ($p = 0.015$; Fig. 4G). Microcracks derived from the main branch were counted as branching. We noted prominent branching in the periosteal region; the degree of branching tended to be greater in the T1DM group than in the control group, but this difference was not statistically significant ($p = 0.059$; Fig. 4H).

4. Discussion

Patients with T1DM have a six-fold higher risk of hip fracture [39] than patients without T1DM; this difference cannot be explained solely by the lower BMD of the former group, as current fracture predictors based on BMD underestimate the burden of fractures in individuals with T1DM. We have utilized multiscale imaging approaches in our previous studies and determined a cohort of elevated cortical porosity as well as higher advanced glycation endproducts to contribute to bone disease with type two diabetes mellitus (T2DM) [40,41]. Here, combining high-resolution microcomputed tomography, quantitative backscattered electron imaging, confocal laser scanning microscopy with immunohistochemistry (IHC) and static bone histomorphometry, we evaluated

cortical bone quality in T1DM with a focus on osteocyte viability, mineralization, and microdamage accumulation in human samples from the midshaft femur. We analyzed bone samples from eight individuals diagnosed with T1DM and 14 age-matched control individuals. Using this multiscale characterization approach, we found signs of an elevated level of osteocyte apoptosis associated with T1DM. In the periosteal region of the T1DM group, we found a higher accumulation of linear microcracks accompanied by a greater occurrence of fully mineralized osteocyte lacunae. Furthermore, lacunar mineralization was more prominent within the younger osteonal bone of the periosteal region (Fig. 5).

Although low bone turnover is expected in T1DM [14], the rate of bone turnover and the number of bone cells are already low in the cortical bone compared with the trabecular bone compartment [42], which hinders the identification of intergroup differences between the T1DM and control groups. Moreover, clinical studies have pointed to reduced BMD in T1DM; however, we did not find differences in vertebral BMD on *ex vivo* DXA scans or in the femoral cortical geometric indices, which is consistent with a previous study [43]. Microarchitectural changes in T1DM bone are more apparent in individuals with diabetic complications, as suggested by Shanbhogue and colleagues, which might explain these discrepancies [44].

To better capture remodeling activity, we investigated osteocyte viability parameters in the cortical bone rather than the metabolically active trabecular bone. Osteocyte apoptosis with fatigue microcracking induces targeted activation of new resorption centers in bone tissue, as first demonstrated by Cordoso et al. [45]. *In vitro* studies and animal studies [46,47] have shown that high glucose

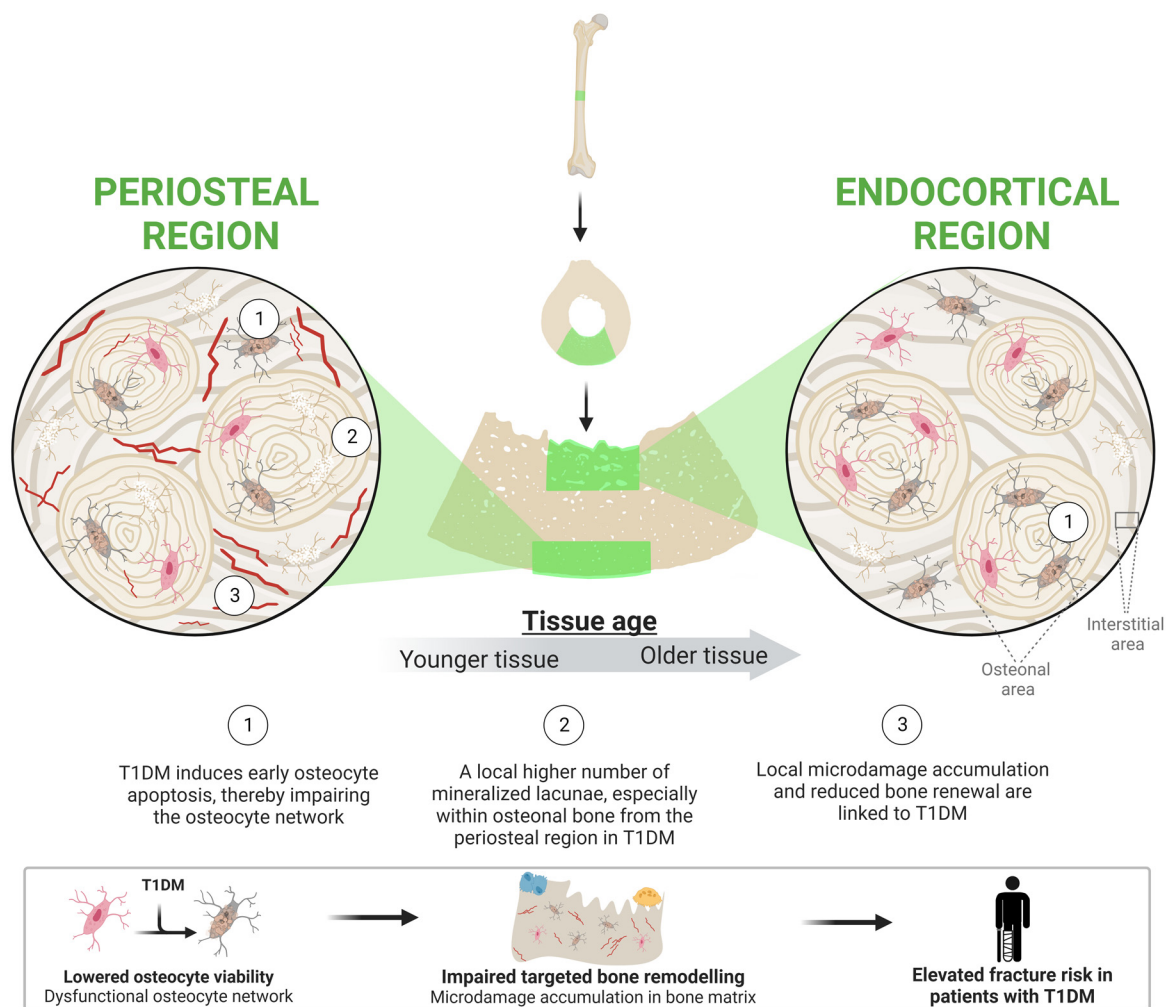


Fig. 5. The effects of T1DM on bone fragility. Increased osteocyte death accompanied by a higher level of mineralized lacunar occlusion contributes to a decreased ability to detect and repair microdamage, leading to a failure and delay or prevention of the remodeling process in the diabetic cortical bone remodeling process.

or diabetes can increase osteocyte apoptosis. Although the TUNEL data did not reveal statistically significant intergroup differences, they indicated a potential trend of elevated osteocyte apoptosis in the T1DM group. Therefore, it was necessary to pair the TUNEL assay with a more sensitive approach to quantify apoptosis. The DNA fragmentation detected by the TUNEL assay might also be found in nonapoptotic cells, i.e., cells undergoing DNA repair [48]; the caspase-3 assay has superior sensitivity [37]. The sensitivity advantage of the caspase-3 assay might also be due to DAB detection, which provides signal amplification. With caspase-3 IHC, we showed that apoptosis of osteocytes in human cortical bone was significantly higher in T1DM patients than in healthy controls.

In our previous work, we showed that occlusion of osteocyte lacunae with mineral aggregates, a phenomenon termed micropetrosis, is pronounced in aged human bone and could therefore be associated with increased fracture risk [17,25]. In the current study, we distinguished between partially and fully mineralized osteocyte lacunae, as partially mineralized lacunae are considered a preliminary step toward fully mineralized lacunae. In addition, partially mineralized lacunae may not necessarily reach the complete mineralization stage (full mineralization of the lacunae) because they can still be removed during remodeling. In contrast, fully mineralized osteocyte lacunae are recognized as the endpoint of micropetrosis events. With aging, the accumulation of mineralized lacunae preferentially occurs in the endocortical region compared

with the periosteal region, as we showed in our previous study [17]. The younger tissue age of the entire periosteal region is due to the apposition of new bone matrix in this region during aging [49]. Geometric cross-section indices were not lower in the T1DM group than in the age-matched control group, meaning that the process of periosteal apposition appears not to be affected by T1DM. In the current study, we observed an elevated number of micropetrosis lacunae in the osteonal bone at the periosteal region of the T1DM group compared with the healthy control group, which is counterintuitive in light of the younger bone tissue. Increased osteocyte apoptosis, leading to reduced numbers of viable osteocytes and increased micropetrosis, negatively affects the mechanical properties of bone. Specifically, a higher number of micropetrosis lacunae leads to a more brittle bone matrix [50,51], which is more prone to microcracking. Our results indeed show an increased number and length of linear microcracks per bone area in the periosteal region in the T1DM group compared to the control group. Therefore, we hypothesize that T1DM induces early osteocyte cell death, causing dysfunction of the osteocyte network, which may impair targeted bone remodeling and result in lower microcrack removal and therefore elevated microcrack accumulation in the cortical bone of T1DM.

Finally, we used high-resolution imaging of the cortical bone to compare the osteonal and interstitial areas of both the periosteal and endosteal regions. Osteonal areas consist of 'younger' bone,

whereas interstitial areas consist of ‘older’ bone. Older interstitial bone tends to have a more mineralized matrix than younger osteonal bone [52,53]. A novel finding from our BMDD analysis was that T1DM patients and controls had similar differences in mineralization levels between younger osteonal bone and older interstitial bone. Furthermore, we found differences between T1DM patients and healthy controls in these osteonal and interstitial areas within the periosteal region: the number of micropetrotic lacunae in the osteonal bone area was higher in T1DM patients than in controls. With aging, the older interstitial bone areas show a higher degree of bone mineralization, and these highly mineralized bone packets are characterized by a limited supply of nutrients, which allows increased accumulation of micropetrotic lacunae compared with younger bone within osteons [17,18]. Interestingly, we observed an increased number of micropetrotic lacunae within the osteonal, younger areas in the periosteal region of T1DM group. Therefore, we hypothesize that T1DM might accelerate the cellular aging processes and lead to the premature death of osteocytes, thereby causing prominent lacunar mineralization, as shown in the osteonal bone of the periosteal region in the T1DM group.

Our study has a few limitations. As human bone material was collected during autopsy, the bone was not labeled with fluorescent markers to enable the assessment of dynamic bone formation indices. However, all specimens were obtained during autopsy exclusively for the purpose of multiscale bone quality assessment. Therefore, anatomical orientation and positioning of the regions of interest could be controlled, facilitating normalizing procedures and high data reproducibility. Deidentified data of the donors did not contain information about diabetes disease onset or duration because of the postmortem origin of the specimens. However, due to the known course of T1DM, we assume an early onset of the disease in childhood or young adulthood with insulin supplementation in donors with T1DM. We collected rare femoral cross-sections during autopsy, allowing us to use an exceptionally large region of interest for the quantitative bone quality assessment. Here, we focused on the anterior quadrant to provide data at a high spatial resolution. Additionally, the anterior quadrant ensures no influence of muscle and tendon attachments on the bone microstructure. The alterations in LCN were deduced based on direct morphological changes in the bone matrix caused by mineralization of lacunae, apoptosis of osteocytes, and linear microcracks. While the predictions of our deep learning model for mineralized lacunae detection are not perfect, the results are generally promising and have practical value within the context of the work. The difficulty in clearly identifying partially mineralized lacunae is reflected in the relatively low accuracy for this class. However, it must be noted that the same difficulty affects human experts, i.e., the labels may be less reliable than those of fully mineralized or nonmineralized lacunae. In fact, the deterministic nature of the learned model presents an advantage in our setting, where the distinction between the three classes is made in the same way for all lacunae. Despite these potential limitations, our study provides new and critical insight into how T1DM affects bone quality and offers evidence for the underlying mechanism of diabetic bone disease in human cortical bone.

5. Conclusion

In summary, the current study highlights osteocyte apoptosis as a potential determinant of cortical T1DM pathology. Osteocyte apoptosis was more frequent in both endocortical and periosteal regions in our T1DM cohort. In addition, we found increased mineralized lacunae in the osteonal area of the periosteal region, signifying that the osteocyte network was disrupted by hypermineralized calcified matter. The accompanying elevated microcrack accu-

mulation in the periosteal region further highlights impaired bone quality in T1DM. Although the periosteal region is considered to consist of younger bone than the endocortical region, we determined that the periosteal region in T1DM is the preferential site for fully mineralized lacunar spaces and microdamage accumulation, which would be more expected in the endocortical region of older bone. In addition, T1DM led to preferential micropetrosis in osteonal areas of the periosteal region, pointing toward osteocyte pathology within newly formed bone. These findings suggest that T1DM accelerates the aging effects in the bone matrix and leads to the premature death of osteocytes.

Data availability statement

The data that support the findings of this study are available upon reasonable request from the corresponding author BB. The data are not publicly available due to privacy concerns or ethical restrictions.

Funding

This project has received funding from the European Union's Horizon 2020 research and innovation program under the Marie Skłodowska-Curie grant agreement no. 860898 to LCH, MR, BB, and KJR. BB receives funding from the German Research Foundation (DFG) under BU2562/10-1. KJR receives funding from German Cancer Aid (Deutsche Krebshilfe) under MSNZ Hamburg HaTRICS4. LH received funding from the Elisabeth-Bonhoff-Foundation. PM received funding from the Ministry of Science of the Republic of Serbia and from the Science Fund of the Republic of Serbia.

Author contributions

SDK, KJ-R, and BB designed the study. BW, HM, KP and BO carried out autopsies and evaluated patient data. SDK and EMW prepared the specimens for ex vivo analysis. SDK, EMW and KJ-R designed and performed experiments and analyzed the data. MN performed experiments. AVF processed the imaging data. SDK performed the statistical analysis. SDK, EMW, HH, PM, LCH, MR, AV, AS, BB and KJ-R interpreted the data. SDK, KJ-R and BB wrote the manuscript. All authors approved the final version of the manuscript.

Disclosure

The authors have no conflicts of interest to declare. All coauthors have seen and agree with the contents of the manuscript, and there is no financial interest to report. We certify that the submission is original work and is not under review at any other publication.

Declaration of Competing Interest

The authors declare that they have no known competing financial interests or personal relationships that could have appeared to influence the work reported in this paper.

The authors declare the following financial interests/personal relationships which may be considered as potential competing interests:

CRediT authorship contribution statement

Sofie Dragoun Kolibová: Conceptualization, Methodology, Investigation, Formal analysis, Writing – original draft, Writing – review & editing. **Eva Maria Wölfel:** Conceptualization, Investigation, Writing – review & editing. **Haniyeh Hemmatian:** Investigation, Writing – review & editing. **Petar Milovanovic:** Investigation,

Writing – review & editing. **Herbert Mushumba:** Investigation. **Birgit Wulff:** Investigation. **Maximilian Neidhardt:** Investigation. **Klaus Püschel:** Investigation. **Antonio Virgilio Failla:** Investigation. **Annegreet Vlug:** Investigation. **Alexander Schlaefer:** Investigation. **Benjamin Ondruschka:** Investigation. **Michael Amling:** Investigation. **Lorenz C. Hofbauer:** Investigation, Writing – review & editing. **Martina Rauner:** Investigation, Writing – review & editing. **Björn Busse:** Conceptualization, Methodology, Investigation, Writing – review & editing. **Katharina Jähn-Rickert:** Conceptualization, Methodology, Investigation, Writing – review & editing.

Acknowledgments

The authors thank Sandra Perkovic and Dr. Imke Fiedler (Department of Osteology and Biomechanics, University Medical Center Hamburg-Eppendorf) and Dr. Bernd Zobiak (UKE Microscopy Imaging Facility, University Medical Center Hamburg-Eppendorf) for their technical and scientific support.

Supplementary materials

Supplementary material associated with this article can be found, in the online version, at doi:10.1016/j.actbio.2023.02.037.

References

- [1] , in: *International Diabetes Federation. IDF Diabetes Atlas, 10th ed., International Diabetes Federation, Brussels, Belgium, 2021, p. 2021.*
- [2] L.A. DiMeglio, C. Evans-Molina, R.A. Oram, Type 1 diabetes, *Lancet* 391 (2018) 2449–2462, doi:10.1016/S0140-6736(18)31320-5.
- [3] M. Mobasser, M. Shirmohammadi, T. Amiri, N. Vahed, H. Hosseini Fard, M. Ghajazadeh, Prevalence and incidence of type 1 diabetes in the world: a systematic review and meta-analysis, *Health Promot. Perspect.* 10 (2020) 98–115, doi:10.34172/hpp.2020.18.
- [4] V.N. Shah, C.S. Shah, J.K. Snell-Bergeon, Type 1 diabetes and risk of fracture: meta-analysis and review of the literature, *Diabet. Med.* 32 (2015) 1134–1142, doi:10.1111/dme.12734.
- [5] T. Vilaca, M. Paggiosi, J.S. Walsh, D. Selvarajah, R. Eastell, The effects of Type 1 diabetes and diabetic peripheral neuropathy on the musculoskeletal system: a case-control study, *J. Bone Miner. Res.* (2021), doi:10.1002/jbmr.4271.
- [6] T. Vilaca, M. Schini, S. Harnan, A. Sutton, E. Poku, I.E. Allen, S.R. Cummings, R. Eastell, The risk of hip and non-vertebral fractures in type 1 and type 2 diabetes: A systematic review and meta-analysis update, *Bone* 137 (2020) 115457, doi:10.1016/j.bone.2020.115457.
- [7] M. Janghorbani, R.M. van Dam, W.C. Willett, F.B. Hu, Systematic review of type 1 and type 2 diabetes mellitus and risk of fracture, 166 (2007) 495–505, doi:10.1093/aje/kwm106.
- [8] H. Fang, L. Huang, I. Welch, C. Norley, D.W. Holdsworth, F. Beier, D. Cai, Early changes of articular cartilage and subchondral bone in the DMM mouse model of osteoarthritis, *Sci. Rep.* (2018), doi:10.1038/s41598-018-21184-5.
- [9] P.J. Lopez-Ibarra, M.M. Pastor, F. Escobar-Jimenez, M.D. Pardo, A.G. Gonzalez, J.D. Luna, M.E. Requena, M.A. Diosdado, Bone mineral density at time of clinical diagnosis of adult-onset type 1 diabetes mellitus, *Endocr. Pract.* 7 (2001) 346–351, doi:10.4158/EP.7.5.346.
- [10] C. Eller-Vainicher, V. Zhukouskaya, Y. v. Tolkachev, S.S. Koritko, E. Cairoli, E. Grossi, P. Beck-Peccoz, I. Chiodini, A.P. Shepelkevich, Low bone mineral density and its predictors in type 1 diabetic patients evaluated by the classic statistics and artificial neural network analysis, *Diabetes Care* 34 (2011) 2186–2191, doi:10.2337/dc11-0764.
- [11] A. Joshi, P. Varthakavi, M. Chadha, N. Bhagwat, A study of bone mineral density and its determinants in type 1 diabetes mellitus, *J. Osteoporos.* 2013 (2013) 397814, doi:10.1155/2013/397814.
- [12] N. Soto, R. Pruzzo, F. Eyzaguirre, G. Iniguez, P. Lopez, J. Mohr, F. Perez-Bravo, F. Cassorla, E. Codner, Bone mass and sex steroids in postmenarcheal adolescents and adult women with Type 1 diabetes mellitus, *J. Diabetes Complicat.* 25 (2011) 19–24, doi:10.1016/j.jdiacomp.2009.10.002.
- [13] K. Hygum, J. Starup-Linde, T. Harsløf, P. Vestergaard, B.L. Langdahl, Mechanisms in Endocrinology: diabetes mellitus, a state of low bone turnover – a systematic review and meta-analysis, *Eur. J. Endocrinol.* 176 (2017) R137–R157, doi:10.1530/eje-16-0652.
- [14] L.J. Raggatt, N.C. Partridge, Cellular and molecular mechanisms of bone remodeling, *J. Biol. Chem.* 285 (2010) 25103–25108, doi:10.1074/jbc.r109.041087.
- [15] L.F. Bonewald, The amazing osteocyte, *J. Bone Miner. Res.* 26 (2011) 229–238, doi:10.1002/jbmr.320.
- [16] P.R. Buenzli, N.A. Sims, Quantifying the osteocyte network in the human skeleton, *Bone* 75 (2015) 144–150, doi:10.1016/j.bone.2015.02.016.
- [17] B. Busse, D. Djonic, P. Milovanovic, M. Hahn, K. Püschel, R.O. Ritchie, M. Djuric, M. Amling, Decrease in the osteocyte lacunar density accompanied by hypermineralized lacunar occlusion reveals failure and delay of remodeling in aged human bone, *Aging Cell* 9 (2010) 1065–1075, doi:10.1111/j.1474-9726.2010.00633.x.
- [18] P. Milovanovic, E.A. Zimmermann, C. Riedel, A. vom Scheidt, L. Herzog, M. Krause, D. Djonic, M. Djuric, K. Püschel, M. Amling, R.O. Ritchie, B. Busse, Multi-level characterization of human femoral cortices and their underlying osteocyte network reveal trends in quality of young, aged, osteoporotic and antiresorptive-treated bone, *Biomaterials* (2015), doi:10.1016/j.biomaterials.2014.12.024.
- [19] R.S. Weinstein, R.W. Nicholas, S.C. Manolagas, Apoptosis of osteocytes in glucocorticoid-induced osteonecrosis of the Hip 1, *J. Clin. Endocrinol. Metab.* 85 (2000), doi:10.1210/jcem.85.8.6714.
- [20] C.C. Kennedy, A. Papaioannou, J.D. Adachi, A. for correspondence, Glucocorticoid-induced osteoporosis, *Women's Health.* 2 (2006) 65–74, doi:10.2217/17455057.2.165.
- [21] T. Rolvien, P. Milovanovic, † Felix, N. Schmidt, S. von Kroge, E.M. Wölfel, M. Krause, B. Wulff, K. Püschel, R.O. Ritchie, M. Amling, B. Busse, Long-term immobilization in elderly females causes a specific pattern of cortical bone and osteocyte deterioration different from postmenopausal osteoporosis, (2020), doi:10.1002/jbmr.3970.
- [22] L.I. Plotkin, SKELETAL BIOLOGY AND REGULATION (MR FORWOOD AND A ROBLING, SECTION EDITORS) Apoptotic osteocytes and the control of targeted bone resorption, (n.d.), doi:10.1007/s11914-014-0194-3.
- [23] J.Y. Ru, Y.F. Wang, Osteocyte apoptosis: the roles and key molecular mechanisms in resorption-related bone diseases, (n.d.), doi:10.1038/s41419-020-03059-8.
- [24] H.M. Frost, *In vivo* osteocyte death, *J. Bone Jt. Surg. Am.* (1960) 42 A, doi:10.2106/00004623-196042010-00011.
- [25] H.M. Frost, Micropetrosis, *J. Bone Jt. Surg. Am.* (1960) 144–150 42-A <https://www.ncbi.nlm.nih.gov/pubmed/13849862>.
- [26] P. Milovanovic, E.A. Zimmermann, A. vom Scheidt, B. Hoffmann, G. Sarau, T. Yorgan, M. Schweizer, M. Amling, S. Christiansen, B. Busse, The formation of calcified nanospherites during micropetrosis represents a unique mineralization mechanism in aged human bone, *Small* 13 (2017) 1602215, doi:10.1002/smll.201602215.
- [27] P. Milovanovic, B. Busse, Phenomenon of osteocyte lacunar mineralization: indicator of former osteocyte death and a novel marker of impaired bone quality? *Endocr. Connect.* 9 (2020) R70–R80, doi:10.1530/ec-19-0531.
- [28] S. Qiu, D.S. Rao, D.P. Fyhrrie, S. Palnitkar, A.M. Parfitt, The morphological association between microcracks and osteocyte lacunae in human cortical bone, *Bone* 37 (2005) 10–15, doi:10.1016/j.bone.2005.01.023.
- [29] O.D. Kennedy, D.M. Laudier, R.J. Majeska, H.B. Sun, M.B. Schaffler, Osteocyte apoptosis is required for production of osteoclastogenic signals following bone fatigue *in vivo*, *Bone* 64 (2014) 132–137, doi:10.1016/j.bone.2014.03.049.
- [30] O. Verborgt, G.J. Gibson, M.B. Schaffler, Loss of osteocyte integrity in association with microdamage and bone remodeling after fatigue *in vivo*, *J. Bone Miner. Res.* 15 (2000) 60–67, doi:10.1359/jbmr.2000.15.160.
- [31] D. Vashishth, O. Verborgt, G. Divine, M.B. Schaffler, D.P. Fyhrrie, Decline in osteocyte lacunar density in human cortical bone is associated with accumulation of microcracks with age, *Bone* 26 (2000) 375–380 <https://www.ncbi.nlm.nih.gov/pubmed/10719281>.
- [32] X. Liu, W. Li, J. Cai, Z. Yan, X. Shao, K. Xie, X.E. Guo, E. Luo, D. Jing, Spatiotemporal characterization of microdamage accumulation and its targeted remodeling mechanisms in diabetic fatigued bone, *FASEB J.* 34 (2020) 2579–2594, doi:10.1096/fj.201902011r.
- [33] V. Sládek, V. Sabolová, O. Šebesta, T. Zikmund, J. Kaiser, S. Červková, Effect of deriving periosteal and endosteal contours from microCT scans on computation of cross-sectional properties in non-adults: the femur, *J. Anat.* 233 (2018) 381–393, doi:10.1111/joa.12835.
- [34] D.W. Dempster, J.E. Compston, M.K. Drezner, F.H. Glorieux, J.A. Kanis, H. Malluche, P.J. Meunier, S.M. Ott, R.R. Recker, A.M. Parfitt, Standardized nomenclature, symbols, and units for bone histomorphometry: A 2012 update of the report of the ASBMR Histomorphometry Nomenclature Committee, *J. Bone Miner. Res.* 28 (2013) 2–17, doi:10.1002/jbmr.1805.
- [35] G. Jocher, A. Stoken, J. Borovec, NanoCode012, ChristopherSTAN, L. Changyu, Laughing, tkianai, yxNONG, A. Hogan, lorenzomammama, AlexWang1900, A. Chaurasia, L. Diaconu, Marc, wanghaoyang0106, ml5ah, Doug, Durgesh, F. Olngam, Frederik, Guilhen, A. Colmagro, H. Ye, Jacobsolawetz, J. Poznanski, J. Fang, J. Kim, K. Doan, 于力军 L.Y., ultralytics/yolov5: v4.0 - nn.SiLU activations, Weights & Biases logging, PyTorch Hub integration, (2021), doi:10.5281/ZENODO.4418161.
- [36] A. Bressenot, S. Marchal, L. Bezdetsnaya, J. Garrier, F. Guillemin, F. Plénat, Assessment of apoptosis by immunohistochemistry to active caspase-3, active caspase-7, or cleaved PARP in monolayer cells and spheroid and subcutaneous xenografts of human carcinoma, *J. Histochem. Cytochem.* 57 (2009) 289–300, doi:10.1369/jhc.2008.952044.
- [37] W.R. Duan, D.S. Garner, S.D. Williams, C.L. Funckes-Shippy, I.S. Spath, E.A. Blomme, R. Duan, D.S. Garner, S.D. Williams, C.L. Funckes-Shippy, I.S. Spath, E.A. Blomme, Comparison of immunohistochemistry for activated caspase-3 and cleaved cytokeratin 18 with the TUNEL method for quantification of apoptosis in histological sections of PC-3 subcutaneous xenografts, 199 (2003) 221–228, doi:10.1002/path.1289.
- [38] M. Kerschmitzki, W. Wagermaier, P. Roschger, J. Seto, R. Shahar, G.N. Duda, S. Mundlos, P. Fratzl, The organization of the osteocyte network mirrors the extracellular matrix orientation in bone, *J. Struct. Biol.* 173 (2) (2011) 303–311, doi:10.1016/j.jsb.2010.11.014.
- [39] P. Vestergaard, Discrepancies in bone mineral density and fracture risk in pa-

- tients with type 1 and type 2 diabetes—a meta-analysis, *Osteoporos. Int.* 18 (2007) 427–444, doi:[10.1007/s00198-006-0253-4](https://doi.org/10.1007/s00198-006-0253-4).
- [40] E.M. Wölfel, K. Jähn, A.K. Siebels, L.-Y. Ma, G.E. Sroga, A. vom Scheidt, F.N. Schmidt, B. Wulff, H. Mushumba, K. Püschel, M. Amling, D. Vashishth, E. Schaible, P. Milovanovic, E. Zimmermann, B. Busse, In type 2 diabetes mellitus collagen fibril plasticity is altered along with higher glyco-oxidative damage and non-osteoporotic bone mineral density, *Bone Rep.* 13 (2020), doi:[10.1016/j.bonr.2020.100694](https://doi.org/10.1016/j.bonr.2020.100694).
- [41] E.M. Wölfel, I.A.K. Fiedler, S. Dragoun Kolibova, J. Krug, M.C. Lin, B. Yazigi, A.K. Siebels, H. Mushumba, B. Wulff, B. Ondruschka, K. Püschel, C.C. Glüer, K. Jähn-Rickert, B. Busse, Human tibial cortical bone with high porosity in type 2 diabetes mellitus is accompanied by distinctive bone material properties, *Bone* 165 (2022) 116546, doi:[10.1016/j.bone.2022.116546](https://doi.org/10.1016/j.bone.2022.116546).
- [42] J. Compston, L. Skingle, D.W. Dempster, Bone histomorphometry, vitamin D: fourth edition. 1 (2018) 959–973, doi: [10.1016/B978-0-12-809965-0.00053-7](https://doi.org/10.1016/B978-0-12-809965-0.00053-7).
- [43] T. Miazgowski, S. Pynka, M. Noworyta-Zietara, B. Kryzanowska-Świniarska, R. Pikul, Bone mineral density and hip structural analysis in type 1 diabetic men, *Eur. J. Endocrinol.* (2007) 156, doi:[10.1530/eje.1.02309](https://doi.org/10.1530/eje.1.02309).
- [44] V. Shanbhogue, S. Hansen, M. Frost, N.R. Jørgensen, A.P. Hermann, J.E. Henriksen, K. Brixen, Bone Geometry, Volumetric density, microarchitecture, and estimated bone strength assessed by HR-pQCT in adult patients with Type 1 diabetes mellitus, *J. Bone Miner. Res.* 30 (2015), doi:[10.1002/jbmr.2573](https://doi.org/10.1002/jbmr.2573).
- [45] L. Cardoso, B.C. Herman, O. Verborgt, D. Laudier, R.J. Majeska, M.B. Schaffler, Osteocyte apoptosis controls activation of intracortical resorption in response to bone fatigue, *J. Bone Miner. Res.* 24 (2009) 597–605, doi:[10.1359/jbmr.081210](https://doi.org/10.1359/jbmr.081210).
- [46] M. Maycas, K.A. McAndrews, A.Y. Sato, G.G. Pellegrini, D.M. Brown, M.R. Allen, L.I. Plotkin, A.R. Gortazar, P. Esbrit, T. Bellido, PTHrP-derived peptides restore bone mass and strength in diabetic mice: additive effect of mechanical loading, *J. Bone Miner. Res.* 32 (2017) 486–497, doi:[10.1002/jbmr.3007](https://doi.org/10.1002/jbmr.3007).
- [47] S. Portal-Núñez, D. Lozano, L. Fernández De Castro, A.R. de Gortázar, X. Nogués, P. Esbrit, Alterations of the Wnt/b-catenin pathway and its target genes for the N- and C-terminal domains of parathyroid hormone-related protein in bone from diabetic mice, *FEBS Lett.* 584 (2010) 3095–3100, doi:[10.1016/j.febslet.2010.05.047](https://doi.org/10.1016/j.febslet.2010.05.047).
- [48] D.T. Loo, *In situ* detection of apoptosis by the TUNEL assay: an overview of techniques, in: 2011: pp. 3–13. doi: [10.1007/978-1-60327-409-8_1](https://doi.org/10.1007/978-1-60327-409-8_1).
- [49] E. Seeman, P.D. Delmas, Bone quality — The material and structural basis of bone strength and fragility, *N. Engl. J. Med.* 354 (2006), doi:[10.1056/nejmra053077](https://doi.org/10.1056/nejmra053077).
- [50] W.S.S. Jee, *Integrated Bone Tissue Physiology: Anatomy and Physiology, Bone Mechanics Handbook, 2001 Second Edition*.
- [51] T.M. Boyce, R.D. Bloebaum, Cortical aging differences and fracture implications for the human femoral neck, *Bone* (1993) 14, doi:[10.1016/8756-3282\(93\)90209-S](https://doi.org/10.1016/8756-3282(93)90209-S).
- [52] C. Bergot, Y. Wu, E. Jolivet, L.Q. Zhou, J.D. Laredo, V. Bousson, The degree and distribution of cortical bone mineralization in the human femoral shaft change with age and sex in a microradiographic study, *Bone* (2009) 45, doi:[10.1016/j.bone.2009.05.025](https://doi.org/10.1016/j.bone.2009.05.025).
- [53] Y. Wu, C. Bergot, E. Jolivet, L.Q. Zhou, J.D. Laredo, V. Bousson, Cortical bone mineralization differences between hip-fractured females and controls. A microradiographic study, *Bone* (2009) 45, doi:[10.1016/j.bone.2009.04.202](https://doi.org/10.1016/j.bone.2009.04.202).